

Article

Impacts of Sea Surface Temperature Variability in the Indian Ocean on Drought Conditions over India during ENSO and IOD Events

Vaibhav Kumar ¹ , Hone-Jay Chu ^{1,*}  and Abhishek Anand ²

¹ Department of Geomatics, National Cheng Kung University, Tainan City 701401, Taiwan; p68097064@gs.ncku.edu.tw

² Department of Civil Engineering, Indian Institute of Technology Madras, Chennai 600036, India; abhioff13@gmail.com

* Correspondence: honejaychu@geomatics.ncku.edu.tw

Abstract: The characteristics of terrestrial droughts are closely linked to simultaneous fluctuations in climatic factors, notably influenced by sea surface temperature (SST). This study explores the response of vegetation photosynthesis, indicated by solar-induced chlorophyll fluorescence (SIF), in India during the summer monsoon period (JJAS) under drought conditions. Notably, statistically significant associations between SST variations in the tropical Indian Ocean and land-based drought responses (precipitation, temperature, soil moisture, and SIF) were observed, which were attributed to atmospheric teleconnections. The positive phases of El Niño and the Indian Ocean Dipole (IOD) significantly impacted SST, triggering severe droughts in India in 2009 and 2015. The results revealed that positive SST anomalies weaken monsoon flow during the onset period, reducing moisture transmission to the Indian subcontinent. In 2009, the precipitation anomaly showed severe drought conditions (<-1.5) primarily in the northwest, central northeast, and west-central subregions, respectively, with soil moisture deficit and reduced photosynthetic activity (indicated by negative SIF anomalies) mirroring precipitation anomalies. In 2015, moderate to severe drought conditions affected regions primarily in the west-central and peninsular areas, with corresponding consistency in SIF anomalies and soil moisture deficits. These conditions led to decreased photosynthetic rates and negative SIF anomalies observed across India. The findings provide insights for predicting droughts and understanding ecosystem impacts across India amidst rapidly changing climate conditions in the Indian Ocean region.

Keywords: El Niño Southern Oscillation; Indian Ocean Dipole; sea surface temperature; drought; solar-induced chlorophyll fluorescence; ocean–atmosphere–vegetation interactions



Citation: Kumar, V.; Chu, H.-J.; Anand, A. Impacts of Sea Surface Temperature Variability in the Indian Ocean on Drought Conditions over India during ENSO and IOD Events. *J. Mar. Sci. Eng.* **2024**, *12*, 136. <https://doi.org/10.3390/jmse12010136>

Academic Editor: Anatoly Gusev

Received: 23 November 2023

Revised: 28 December 2023

Accepted: 5 January 2024

Published: 9 January 2024



Copyright: © 2024 by the authors. Licensee MDPI, Basel, Switzerland. This article is an open access article distributed under the terms and conditions of the Creative Commons Attribution (CC BY) license (<https://creativecommons.org/licenses/by/4.0/>).

1. Introduction

Sea surface temperature (SST), a critical geophysical parameter of the ocean, provides valuable information about the heat content at the ocean surface and plays a fundamental role in influencing the earth's climate [1]. By controlling dynamic and biogeochemical processes that connect the ocean to the atmosphere, this essential oceanic variable significantly affects the weather and climate patterns on our planet [2]. To comprehend the intricate air–sea interactions and their effects on the earth's surface, SST is utilized as a straightforward and reasonable indication. In addition, the changes in SST can exacerbate extreme climatic events that cause significant losses in agriculture and the economy when combined with variations in surface air temperatures [3,4]. By modifying heat and moisture fluxes over the air bridge, some regional SST anomalies regulate the photosynthetic absorption of carbon in terrestrial ecosystems [5,6]. Through teleconnections, climatic oscillations like the El Niño Southern Oscillation (ENSO), Indian Ocean Dipole (IOD), Pacific Decadal Oscillation (PDO), and Atlantic Multidecadal Oscillation (AMO) impact the world's vegetation, demonstrating the importance of the ocean for sustaining terrestrial ecosystems [7–9].

El Niño represents the warming period of the ocean, whereas La Niña represents the cooling phase. When strong westerly winds throughout the Pacific basin blow across it, a significant El Niño is discovered and further intensified by easterly winds [10]. The study carried out by [11] showed that El Niño's development results in rainfall on South America's equatorial coast, convective storms and hurricanes in the central Pacific, and dryness in the western Pacific. A strong El Niño is subsequently followed by La Niña, which reaches the central and eastern Pacific with strong trade winds and cold water. It causes heavy rainfall in eastern Australia, a cold and wet winter in southeast Africa, a winter drought in the southern United States, a strong monsoon in India and Southeast Asia, and a cold winter in western Canada and the northwest of the United States [12–14]. In the last decades, several other studies have also attempted to understand ENSO and its impacts on Indian summer monsoon rainfall (ISMR) variability [15–19]. El Niño (the positive phase of ENSO) events are linked to decreased ISMR because of anomalous subsidence linked to a change in zonal Walker circulation, while La Niña (the negative phase of ENSO) events are linked to conditions of excess rainfall in the Indian region [20]. The study carried out by [21], highlighted that the normal break phase dominates an El Niño year, whereas the typical active phase dominates a La Niña year. The findings of their study indicate that the association between El Niño and breaks is not reliant on the ENSO–monsoon relationship, but the relationship between La Niña and activities is connected to the ENSO–monsoon relationship. The relationship between ENSO and variations in the Walker and Hadley circulations is also well-recognized. By interacting with the equatorial Walker circulation and the regional Hadley circulation, which are regarded as the two most significant and well-known atmospheric zonal and meridional circulations worldwide, ENSO influences the Indian monsoon [22,23]. Ashok and Saji [24] investigated the relative effects of the Indian summer monsoon rainfall (June–September) at sub-regional scales between ENSO and Indian Ocean Dipole (IOD) episodes.

However, the scientific community's primary attention was focused on investigating the processes underlying the ENSO phenomenon, which was thought to be the most significant driver of ISMR variability until the IOD mode was found in the Indian Ocean [25]. The IOD is a phenomenon that occurs in the tropical Indian Ocean and is a result of varying anomalous bi-polar surface temperatures at the ocean's surface [12,25,26]. The irregular oscillation of SST over the Indian Ocean results in periodic warming in the western region and cooling in the eastern region. The positive IOD phase describes this state. Regarding the negative IOD phase, the Indian Ocean's eastern sea is warmer than its western sea. Climate-wise, a positive IOD causes the western Indian Ocean to have higher sea surface temperatures and more precipitation, whereas a negative IOD causes the eastern Indian Ocean to cool down and cause droughts in Australia and Indonesia [11,26]. The studies [25,27] discussed the equatorial Indian Ocean's zonal wind anomalies and east–west SST gradients that are linked to the intensity of IOD. They demonstrated how this mode is intrinsic throughout the Indian Ocean, seasonally phase-locked, and unaffected by ENSO. After the discovery of IOD, several studies were carried out to explore its characteristics, relationship with ENSO, ISMR, and climate of other tropical regions [28–31]. The findings of [28] indicate that the effects of ENSO and the IOD on ISMR are complementary. It has been noticed that during a positive IOD event, there is a notable convergence of airflow over the Bay of Bengal and Indian region. This convergence leads to an increase in precipitation across the Indian region. Numerous studies have shown this teleconnection between ENSO and the IOD with dry/wet conditions over India [32,33]. Furthermore, in the absence of IOD occurrences, the subsidence over the Indian subcontinent generated by ENSO is substituted by a convergence induced by the IOD. This convergence leads to the occurrence of regular summer monsoon rainfall, even in the presence of a strong El Niño event. Similarly, negative IOD episodes have the potential to mitigate the influence of La Niña on ISMR, resulting in a deficiency in monsoon precipitation. According to the findings, the simultaneous occurrence of the IOD and ENSO has the effect of mitigating the influence of ENSO on ISMR. The study [34] conducted an additional investigation,

which revealed that the intensity of IOD occurrences remains consistent regardless of their co-occurrence with ENSO. It has been noted that the occurrence of IOD events can be attributed to the interconnected air–sea interactions that are endemic to the tropical Indian Ocean. Furthermore, it is important to highlight that these events can transpire independently of the ENSO phenomenon.

India has an agricultural-dependent economy where more than 68% of people depend upon agriculture, and its related activities and drought are a vital contributor to India's significant famines [35]. Nearly 62% of the population is employed in the farming sector, and it contributes approximately 16% of India's gross domestic product (Economic Survey 2019–2020). The climate of India is tropical humid type, which is dominated by the southwest monsoon (June to September). India receives approximately 80% of its annual rainfall from June to September (JJAS) because of the southwest monsoon. The all-India averaged rainfall has a minimal inter-annual fluctuation [36]. If the monsoon rainfall shortfall is higher than 10%, the India Meteorological Department (IMD) classifies the year as a drought year. At the same time, the overall rainfall in India remains consistent throughout time [36–38]. Several studies have observed decreased patterns in monsoon-season rainfall across India since 1950, which may have resulted in an increase in the frequency of droughts in India [18,39–42]. Moreover, soil moisture and evapotranspiration strongly contribute to drought identification, while precipitation deficits remain a main driver in normal and flash drought [43].

SST has a crucial role in regulating terrestrial climate as an influential external factor [44], thereby controlling the spatiotemporal distribution of climate factors that, through physiological processes, have a direct impact on drought conditions, e.g., precipitation, temperature, soil moisture, and photosynthetic activity of vegetation [45]. By altering land surface temperature and precipitation, the West Pacific Warm Pool has a strong but erratic impact on net ecosystem productivity in both the northern (negative correlation) and southern (positive correlation) hemispheres [46]. For the most part, plant growth and productivity are governed by hydroclimatic variations [47,48]. The primary focus of past studies has been on examining the impacts of precipitation and temperature on a range of structural and functional attributes of vegetation in India [49,50]. Moreover, studies utilized remote SST forcing to illustrate the influence of ENSO on the inter-annual variability of plant growth in India, as well as the effect of climatic variability on ecosystem services [51–54]. The study conducted by [47] demonstrated the capacity to forecast anomalies in the NDVI throughout India by utilizing soil moisture and the ENSO index. In addition, the influence of ENSO teleconnections is accompanied by the variability in SST in the tropical Indian Ocean, which further plays a role in the occurrence of vegetation anomalies in India [9].

To comprehend how drought responds to ocean variability in the influence of ENSO and the IOD, a thorough investigation is required to observe the relationship between SST variations and drought conditions, such as land surface variables, especially terrestrial photosynthesis, in terms of solar-induced chlorophyll fluorescence (SIF) anomalies [55]. As a result of the time lag between each link in this cause-and-effect chain, SST indices are more predictive of terrestrial photosynthesis variability than meteorological factors [56]. Several studies have shown that plant greenness in the dry and semi-arid climatic zones of the tropical belt may be predicted three to six months ahead of time using SST [45]. Here, the primary objective of this study is to use SST indices to examine how anomalies in precipitation, temperature, soil moisture, and vegetation photosynthesis over the Indian subcontinent are influenced by the tropical Indian Ocean during ENSO and IOD events. For this, our analysis is focused on teleconnections between SST and drought variables during the monsoon period (June to September) by selecting two contrasting years (herein, 2009 and 2015; Appendix A). The peculiar dynamics of these two years were not fully investigated. Notably, 2009 was an El Niño year, and 2015 was recorded as a strong El Niño year with a positive IOD. The Indian landmass region experienced below-normal rainfall, which caused severe droughts.

2. Study Area and Materials

This study was carried out over the Tropical Indian Ocean, which is characterized by three major basins, namely, the western Indian Ocean (WIO), central Indian Ocean (CIO), and northern Indian Ocean (NIO), respectively (Figure 1). This division is based on the observed spatial distribution of average seasonal SST during the summer monsoon period [57]. The bathymetry profile of ocean basins depicted the depths of ocean beds (in meters). This was retrieved from the GEBCO gridded bathymetry data at the British Oceanographic Data Centre (BODC) (https://www.gebco.net/data_and_products/gridded_bathymetry_data/) (accessed on 16 October 2023). The Indian Ocean shares its land boundary on three sides with the Indian landmass. India is a mega-diverse country that spans its latitudinal boundary from 8–38° N and longitudinal boundary 66–100° E (more than 44% area is agricultural land). Based on the IMD homogenous precipitation zones, the entire country is classified into six zones, namely, the Himalayan Region (HR), northeast (NE), northwest (NW), central northeast (CNE), west-central (WC), and the Peninsular region (PR), respectively.

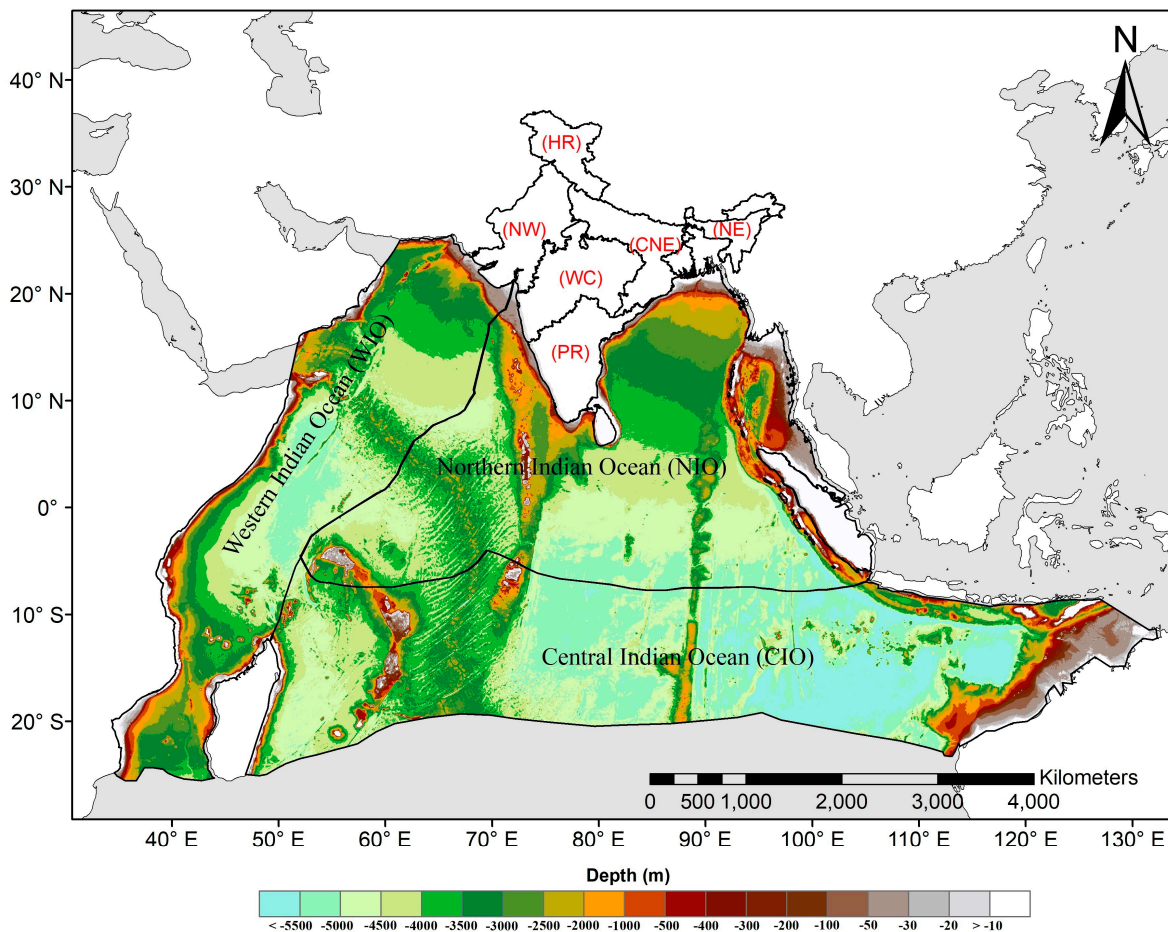


Figure 1. Study area with the bathymetry profile of three Indian Ocean basins, namely, the western Indian Ocean (WIO), northern Indian Ocean (NIO), and central Indian Ocean (CIO), respectively.

2.1. Sea Surface Temperature (SST)

The SST dataset was acquired from NOAA Optimum Interpolation Sea Surface Temperature version 2 (OISST v2). The OISST v2 dataset is widely recognized as a prominent Level 4 (L4) dataset, which is created by integrating satellite observations and in situ data on a consistent worldwide grid. To address missing values, an interpolation technique is used [58–60]. Over a period of 22 years (2001–2022), a monthly mean climatology was established, and the anomalies in SST were acquired. Table 1 shows overview of the datasets used in this study.

2.2. Wind Components

To examine the circulation characteristics and moisture transport related to the summer monsoon, the zonal and meridional wind components at the 850 hPa level were utilized. The wind components for the Indian Ocean throughout the specified period (2001–2022) were extracted from the European Centre for Medium-Range Weather Forecasts (ECMWF) reanalysis dataset known as ERA5 [61–63].

2.3. Precipitation and Temperature

Daily long-term (1901–2022) precipitation data were obtained from the India Meteorological Department, which are available at $0.25^\circ \times 0.25^\circ$ of spatial resolution. The inverse distance weighting interpolation scheme [64] was used to generate this gridded precipitation utilizing a 6995-rain gauge station network located across India [65]. The daily gridded mean temperature was also obtained from the IMD, which is available at $(1.0^\circ \times 1.0^\circ)$ of spatial resolution [66]. It is developed using more than 350 stations and an inverse distance weighted method [64]. The spatial variability and climatological aspects of ISMR are well addressed in this gridded precipitation [67]. One study [41] examined this gridded precipitation to generate a drought monitoring index and assessed the variability (i.e., interannual, decadal, and long-term trends) in monsoon droughts over India. Furthermore, orographic precipitation is well addressed in the Himalayan foothills, northeastern India, and the Western Ghats. Several studies have used this gridded precipitation dataset for drought and heatwaves analysis [68–70].

2.4. Root Zone Soil Moisture (RZSM)

Monthly long-term (1980–2022) root zone soil moisture (RZSM) was accessed from the Global Land Evaporation Amsterdam Model (GLEAM) <https://www.gleam.eu/>, which is available at $0.25^\circ \times 0.25^\circ$ of spatial resolution. RZSM represents the ratio between the water volume in a unit soil volume and the total soil volume. The depth of the root zone depends on the land cover type and is divided into three layers for tall vegetation (0–10 cm, 10–100 cm, and 100–250 cm), two layers for low vegetation (0–10 cm and 10–100 cm), and one layer for bare soil (0–10 cm).

The GLEAM is designed to estimate terrestrial evapotranspiration, potential evapotranspiration (PET), and root zone soil moisture (RZSM) primarily with parameterized physical processes [71–73]. The Priestley and Taylor algorithm [74] is used to estimate potential evapotranspiration (PET), utilizing significant independent remote sensing measurements as model inputs. These inputs include vegetation optical depth, soil moisture, and the snow water equivalent. The empirical parameters utilized in this equation, such as the latent heat of evaporation and the evaporation stress factor, are derived from research in several domains. In addition, the RZSM is based on a multi-layer running water balance [71,72]. In contrast with conventional land models like those in ERA5 and GLDAS, the GLEAM is driven by satellite data to provide RZSM estimations. Consequently, the GLEAM provides a higher degree of independence compared with reanalysis products such as GLDAS and ERA5.

2.5. SIF

To generate SIF anomalies, the Global Ecology Group Data Repository was accessed (<http://data.globalecology.unh.edu/>). The GOSIF dataset provides global coverage, which is available at $0.05^\circ \times 0.05^\circ$, with three temporal periods, i.e., 8 days, monthly, and annual, respectively [75]. The GOSIF is measured in units of $W m^{-2} \mu m^{-1} sr^{-1}$ and developed using a data-driven approach combining discrete OCO-2 SIF soundings, remote sensing data from the Moderate-Resolution Imaging Spectroradiometer (MODIS), and meteorological reanalysis data using regression tree model [76,77]. This GOSIF product showed its usefulness by capturing the crop regions with the highest daily productivity at the global scale. Due to its mechanical link to internal photosynthetic processes, SIF is a better indication of real plant photosynthesis than traditional greenness-based vegetation

indices, e.g., NDVI and EVI, which measure vegetation greenness [78–80]. These indices have been used extensively to track vegetation stress during short- and long-term drought episodes [81,82]. It is challenging to precisely capture plant responses to environmental stressors using VIs on a short-term scale.

Table 1. Overview of the datasets used in this study from 2001 to 2022 with the products’ original specifications.

Data	Source	Spatial Resolution	Temporal Resolution	Reference
Sea surface temperature (SST)	NOAA PSL	0.25° × 0.25°	Monthly	[83]
Wind components at 850 hPa	ERA 5	0.25° × 0.25°	Monthly	[63]
Precipitation	IMD	0.25° × 0.25°	Daily	[65]
Surface air temperature (T2m)	IMD	1.0° × 1.0°	Daily	[66]
Root zone soil moisture (RZSM)	GLEAM 3.8a	0.25° × 0.25°	Monthly	[71]
Solar-Induced chlorophyll Fluorescence (SIF)	GOSIF v2	0.05° × 0.05°	Monthly	[75]

3. Methodology

Firstly, all the datasets from 2001 to 2022 were resampled as 0.25° × 0.25° of spatial resolution using bilinear interpolation and converted to the monthly scale for the monsoon season (June to September) to generate anomalies for SST, precipitation, root zone soil moisture (RZSM), surface air temperature (T2m), and solar-induced chlorophyll fluorescence (SIF).

3.1. Computation of SST Anomalies and Drought Variables

The standardized function of Y , such as SST, rainfall, RZSM, T2m, or SIF, is calculated using the following equation:

$$Y(m, n, t)' = \frac{Y(m, n, t) - \bar{Y}(m, n)}{std(Y(m, n))} \tag{1}$$

where $Y(m, n, t)'$ is the standardized value of pixel (m, n) at time t ; $Y(m, n, t)$ is the original value of pixel (m, n) at time t ; $\bar{Y}(m, n)$ is the mean value of pixel (m, n) during the period from 2001 to 2022, and $std(Y(m, n))$ is the standard deviation of pixel (m, n) from 2001 to 2022.

An SST anomaly (SSTA) is identified by the condition where the standardized SST value is lower than -1 . Table 2 depicted the drought classification. Drought is classified based on standardized rainfall, RZSM, and SIF. A drought event is identified by the condition where a grid cell is under moderate drought conditions when standardized rainfall, RZSM, and SIF are lower than -1 (e.g., rainfall, RZSM, and SIF anomalies). Furthermore, the T2m anomaly profile is the inverse of the other drought variables. In drought conditions, above-normal temperatures lead to increased soil moisture evaporation and water loss from vegetation.

3.2. Wind Speed Visualization

To examine the circulation characteristics and moisture transport during the monsoon period, the wind speed was calculated using the following equation:

$$ws = \sqrt{(u^2 + v^2)} \tag{2}$$

where u and v are the zonal and meridional components of wind, respectively [84].

Table 2. Drought classification based on standardized rainfall, RZSM, and SIF.

Category for Drought	Category	Value
No drought	Extremely wet	≥ 2.00
	Severely wet	1.50 to 1.99
	Moderately wet	1.00 to 1.49
	Mild wet	0.00 to 0.99
Mild drought	Mild drought	−0.99 to 0.00
Moderate drought	Moderate drought	−1.49 to −1.00
Severe drought	Severe drought	−1.99 to −1.50
	Extreme drought	≤ -2.00

3.3. Measurement of NINO 3.4 and DMI

To observe the influence of ENSO, the NINO 3.4 index was used. The NINO 3.4 index refers to the sea surface temperature (SST) anomalies that are calculated by averaging the SST values in the Niño 3.4 region (5° S–5° N, 170°–120° W). It is calculated using data from the global climate observation system provided by the NOAA Physical Sciences Laboratory (PSL) [83]. In addition, the magnitude of the IOD is measured with the dipole mode index (DMI). It is computed as $DMI = SSTA_{(IOD\ west)} - SSTA_{(IOD\ east)}$, where $SSTA_{(IOD\ west)}$ is the SST anomaly in the tropical west Indian Ocean (10° S–10° N, 50° E–70° E) and $SSTA_{(IOD\ east)}$ is the SST anomaly in the tropical southeastern Indian Ocean (10° S–0° S, 90° E–110° E). The DMI dataset was obtained from the NOAA Physical Sciences Laboratory (PSL) [85].

4. Results

4.1. Seasonal SST Variations

Figure 2 illustrates the seasonal SST climatology for 22 years derived from the OISST dataset across the Indian Ocean. The combined impacts of oceanic and atmospheric circulation, as well as oceanic and atmospheric processes at the air–sea interface (which are primarily governed by seasonal variations in incoming solar radiation), produce strong seasonality in the SST. The monsoons in the Arabian Sea follow an annual cycle that is characterized by a bimodal distribution. These monsoons have a substantial impact on the upper thermal structure, which plays a crucial role in regional circulation and the movement of heat and salt. The SST follows an annual cycle that primarily consists of four stages including (1) warming (February–May), (2) cooling (May–August), (3) warming (August–October), and (4) cooling (October–January) over the WIO or Arabian sea [86]. In contrast, most other ocean basins only exhibit two phases in their yearly SST cycle: warming in the pre-summer and summer and cooling in the autumn and winter. The atypical behavior exhibited by the Arabian Sea can be attributed to the prevailing southwest monsoon, which holds sway over the region during the summer season in the northern hemisphere.

The surface seawater in the WIO, CIO, and NIO experienced cooler temperatures during December–January–February, fluctuating between 22 °C and 26 °C. However, the temperature started escalating from March to May, and above 30 °C, it dominated in the WIO and NIO regions, signifying the development of a southwest monsoon over the tropical Indian Ocean. The pre-monsoon (March to May) warmth was probably caused by lower winds, a clear sky, and more solar insolation that was absorbed in the upper layer. This resulted in thermal stratification and restricted turbulent mixing. This can be likened to the inhibition of turbulent kinetic energy [87]. From April to August, the WIO and NIO regions experienced warmer SST, which ranged between 28 °C and 30 °C. During this period, the SST increased by 1–2 °C, whereas the CIO region observed lower warming during this period, ranging from 24 °C to 28 °C. In addition, the SST increased by 2–3 °C, respectively. The NIO region emerged as the warmest, with the WIO and CIO regions

trailing closely behind in terms of temperature. Several research studies indicated that sea surface wind and sea surface heat flux are the primary causes of seasonal variations in the SST [88,89]. In addition, the study [90] noted that the intensity of incoming wind and solar radiation can cause the sea surface temperature to rise.

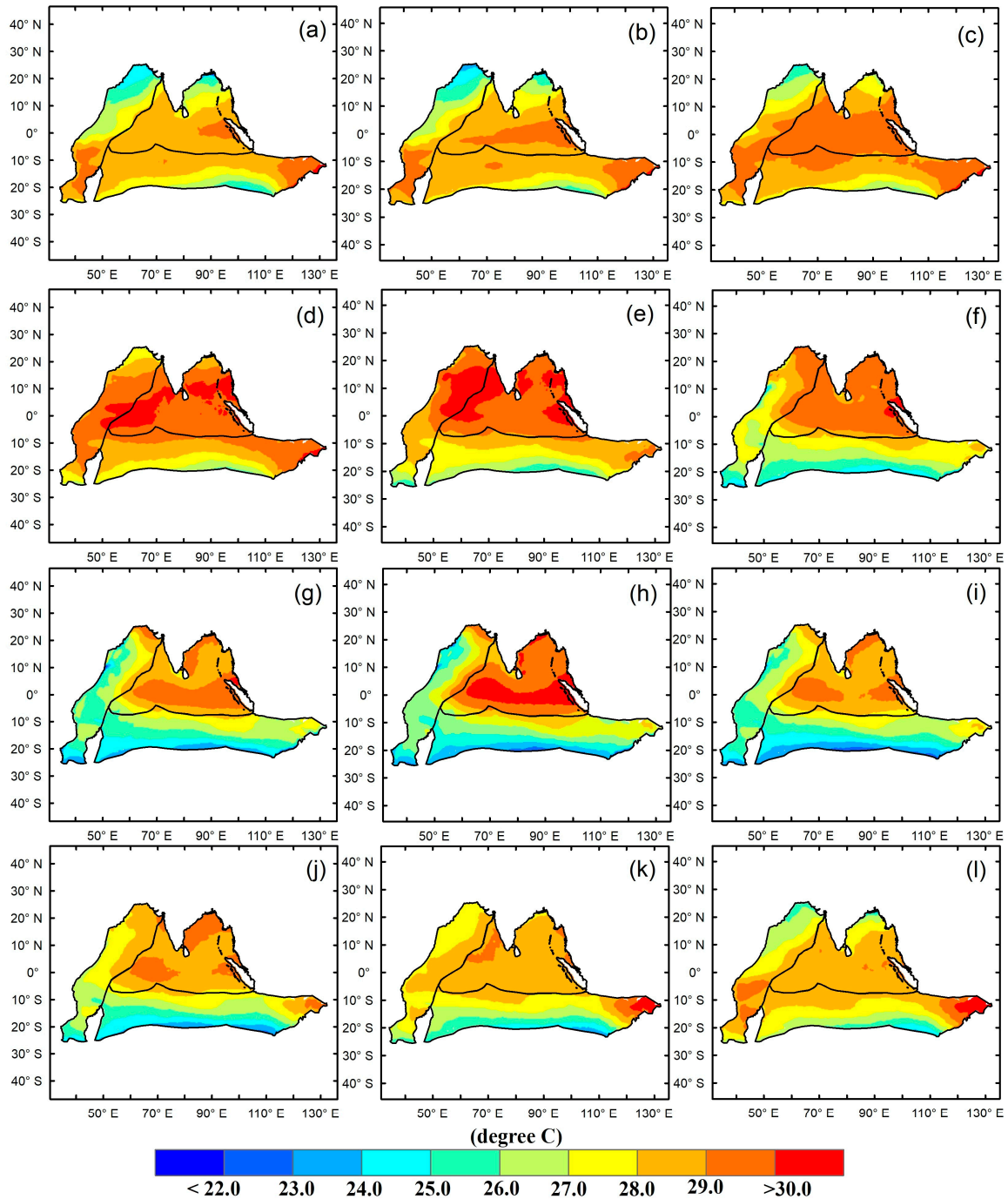


Figure 2. The long-term annual cycle from January to December (a–l) of SST continuous from 2001 to 2022.

4.2. Long-Term Variations in Average SST Anomalies in the WIO, CIO, and NIO

Figure 3 shows the temporal variations in average SST anomalies of the WIO, CIO, and NIO for monsoon months (JJAS) from 2001 to 2022. The SST anomalies reflected warming and cooling trends across the WIO, CIO, and NIO, respectively. The fluctuations in the SST over the WIO, NIO, and CIO appear to exhibit significant interconnections until the year

2013. Following the year 2013, the SST variations in the CIO exhibit a lack of synchrony with the SST anomalies observed in the WIO and NIO. The rate of SST anomalies increased by $0.02\text{ }^{\circ}\text{C}$ in the WIO, $0.04\text{ }^{\circ}\text{C}$ in the NIO, and 0.03 in the CIO, respectively. Thus, the rate of SST anomalies from 2001 to 2022 was observed to be higher in the NIO followed by the WIO and CIO, respectively. This could suggest that the warming and cooling SST variability anomalies in the WIO, CIO, and NIO were caused by the seasonal cycle and inter-annual variability (such as the IOD and ENSO). For the NIO, the warming (maximum) trend crossed $1.0\text{ }^{\circ}\text{C}$, and cooling (minimum) reached $-0.7\text{ }^{\circ}\text{C}$ continuously from 2001 to 2022.

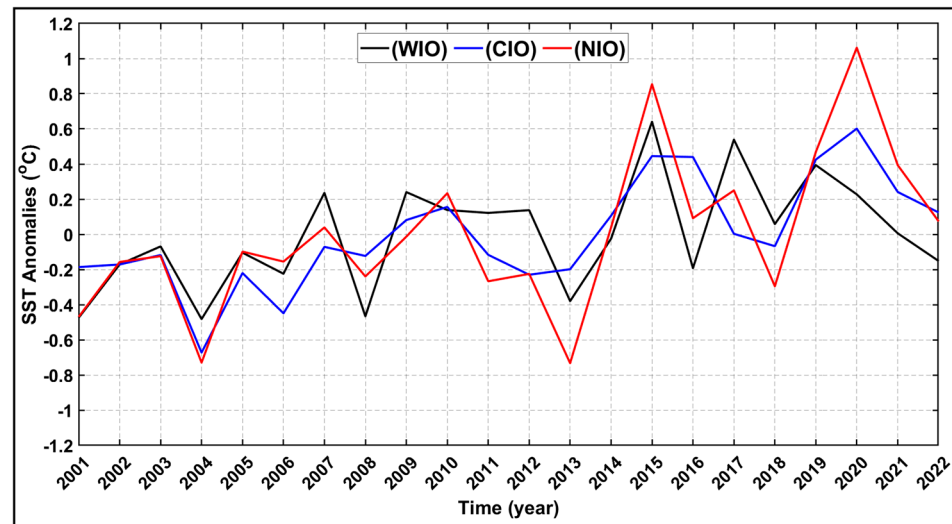


Figure 3. Temporal variations in average SST anomalies in the WIO, CIO, and NIO during the monsoon period (June–September) from 2001 to 2022.

In 2020, the NIO region had a widespread increase in temperature. This unusual warming was a result of an extremely positive IOD event that occurred in the basin. The possible reason for this was well-addressed by [91], who explained an extreme 2019 (IOD) triggered the formation of oceanic downwelling Rossby waves and the warming of the thermocline in the southwest tropical Indian Ocean (TIO). This resulted in the warming of the sea surface via a feedback mechanism between the thermocline and sea surface temperature (SST) from late 2019 to early 2020.

Similarly, for the WIO, the warming (maximum) trend crossed 0.6 and cooling reached (minimum) $-0.5\text{ }^{\circ}\text{C}$ throughout the adapted period. Moreover, the maximum and minimum values reached $0.6\text{ }^{\circ}\text{C}$ and $-0.7\text{ }^{\circ}\text{C}$ of the CIO throughout the adapted period. The increase in SST anomalies over the tropical Indian Ocean has a linkage with climate change and global warming [92].

4.3. SST Anomalies in the Indian Ocean vis-à-vis ENSO Phases and the IOD

The SST anomalies for the WIO, NIO, and CIO regions were computed during the summer monsoon season (June–September) of the El Niño (positive IOD) phases of 2009 and 2015 (see Figures 4 and 5). During the 2009 El Niño years, the SSTA was observed to be higher ($>2.0\text{ }^{\circ}\text{C}$) in the western tropical Indian Ocean (WTIO) (10° S – 10° N , 50 – 70° E), whereas the eastern tropical Indian Ocean (ETIO) (10° S – Eq , 90 – 110° E) region's SSTA ranged between $1.0\text{ }^{\circ}\text{C}$ and $1.5\text{ }^{\circ}\text{C}$ during the onset of the monsoon. A slight decrease in the SST was noted in the WTIO region, and the anomalies ranged between $1.0\text{ }^{\circ}\text{C}$ and $2.0\text{ }^{\circ}\text{C}$ during the monsoon period (July to September). In the Indian Ocean, a weak positive IOD event occurred with a relatively low amplitude from the boreal summer to autumn in 2015, concurrently with a strong El Niño event (amplitude of $1.5\text{ }^{\circ}\text{C}$) over the tropical Pacific Ocean. Typically, a strong IOD episode usually coincides with a strong El Niño event [30].

However, in 2015, the magnitude of the IOD was observed to be weaker. The abnormal spatial pattern in SSTAs in JJAS 2015 showed a positive IOD distribution covering the WTIO and the western to the central Indian Ocean, whereas negative SSTAs was observed in a specific region of the ETIO, west of Sumatra and the central Indian Ocean. During this period, the WTIO region experienced unusual warming and SSTAs crossed above 2.5 °C, whereas SST anomalies fluctuated from 0.5 °C to 1.5 °C over the ETIO region.

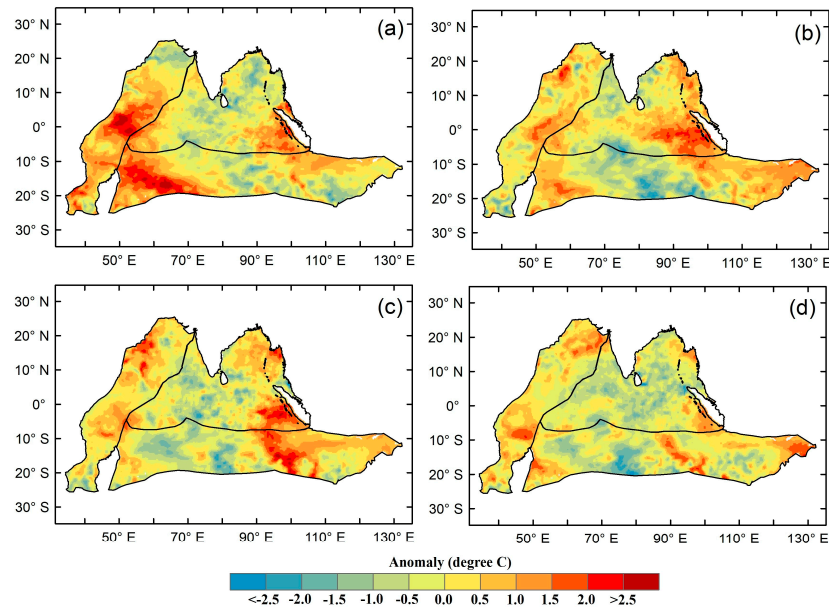


Figure 4. SST anomalies in the WIO, CIO, and NIO for (a) June, (b) July, (c) August and (d) September during 2009 El Niño event.

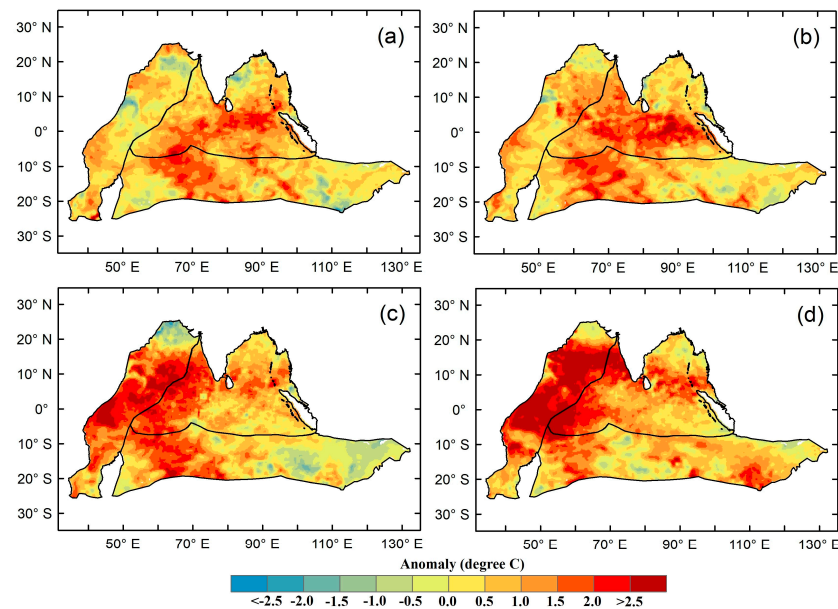


Figure 5. SST anomalies in the WIO, CIO, and NIO for (a) June, (b) July, (c) August and (d) September during 2015 El Niño and positive IOD phase.

4.4. Wind Speed in the Indian Ocean vis-à-vis ENSO Phases and the IOD

The SST and wind showed a significant correlation, indicating a substantial link between the ocean and the atmosphere over the tropical Indian Ocean. Herein, Figures 6 and 7 show the wind speed over the WIO, CIO, and NIO during the monsoon period of 2009 and 2015. The surface wind (resultant v_{10}) was plotted at 10 m above sea surface at 850 hPa

covering the entire three regions (herein, the WIO, CIO, and NIO). However, the wind speed showed an increasing trend as the monsoon set during JJAS 2009. During this period, the wind speed was higher (>20 m/s) in the WIO region, while the NIO region showed the lowest surface wind (2 to 4 m/s). The observed fluctuation patterns underscore the essential influence of wind on SST within the western basin. The mechanisms explaining the air–sea feedback, along with the interaction between wind and thermodynamic parameters, suggest that SST in this region is primarily influenced by the force exerted by the wind. The wind pattern confirms the dramatic and distinct atmospheric response to SSTAs during the JJAS 2009 and 2015 years.

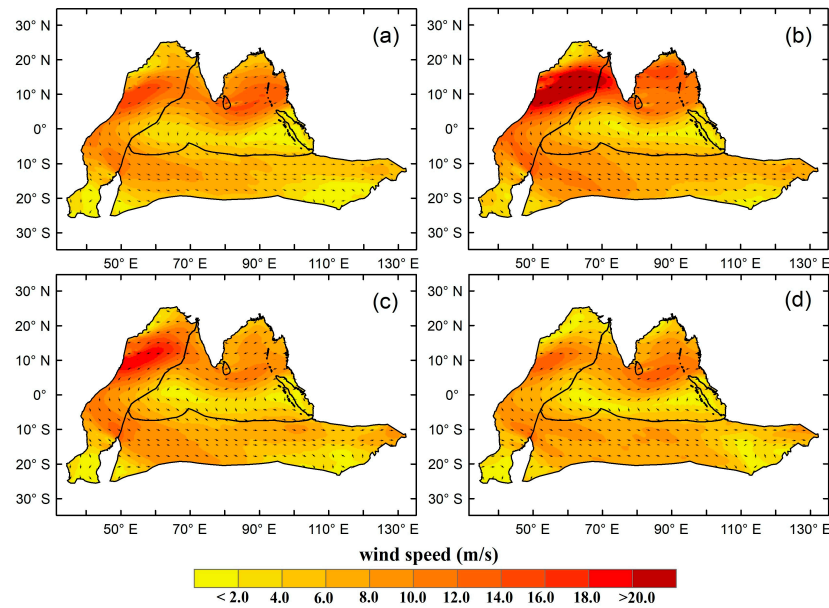


Figure 6. Wind speed and direction in the WIO, CIO, and NIO for (a) June, (b) July, (c) August and (d) September during 2009 El Niño event.

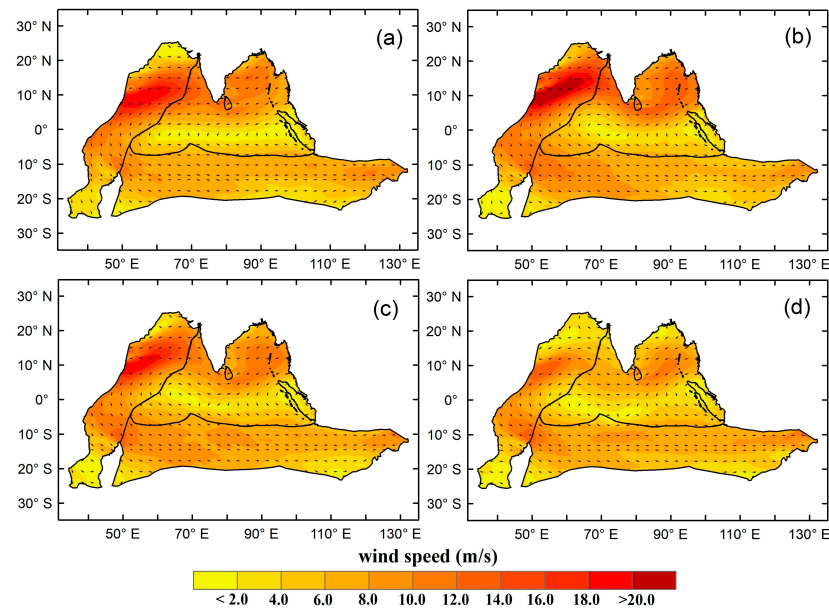


Figure 7. Wind speed and direction in the WIO, CIO, and NIO for (a) June, (b) July, (c) August and (d) September during 2015 El Niño and positive IOD phase.

4.5. Response of Drought Variables

As discussed earlier, anomalies in SST in the Indian Ocean were notably influenced by the El Niño phenomenon in the Pacific Ocean, as well as by the development of weak positive IOD events in the tropical equatorial Indian Ocean during the years 2009 and 2015. These events have an adverse impact on ISMR (Appendix A: rainfall excess/deficit anomaly). Several studies have shown this relationship between SST in the tropical Indian Ocean and the monsoon variability over India and surrounding regions [93–95]. Here, precipitation, surface air temperature (T2m), soil moisture, and SIF anomalies are shown (see Figures 8 and 9) for the monsoon period (June–September) during the 2009 and 2015 drought events. The results revealed that all anomalies (herein, precipitation, T2m, and SM) are mostly consistent (in terms of severity and geographical extent) and indicate drought conditions across the six sub-regions.

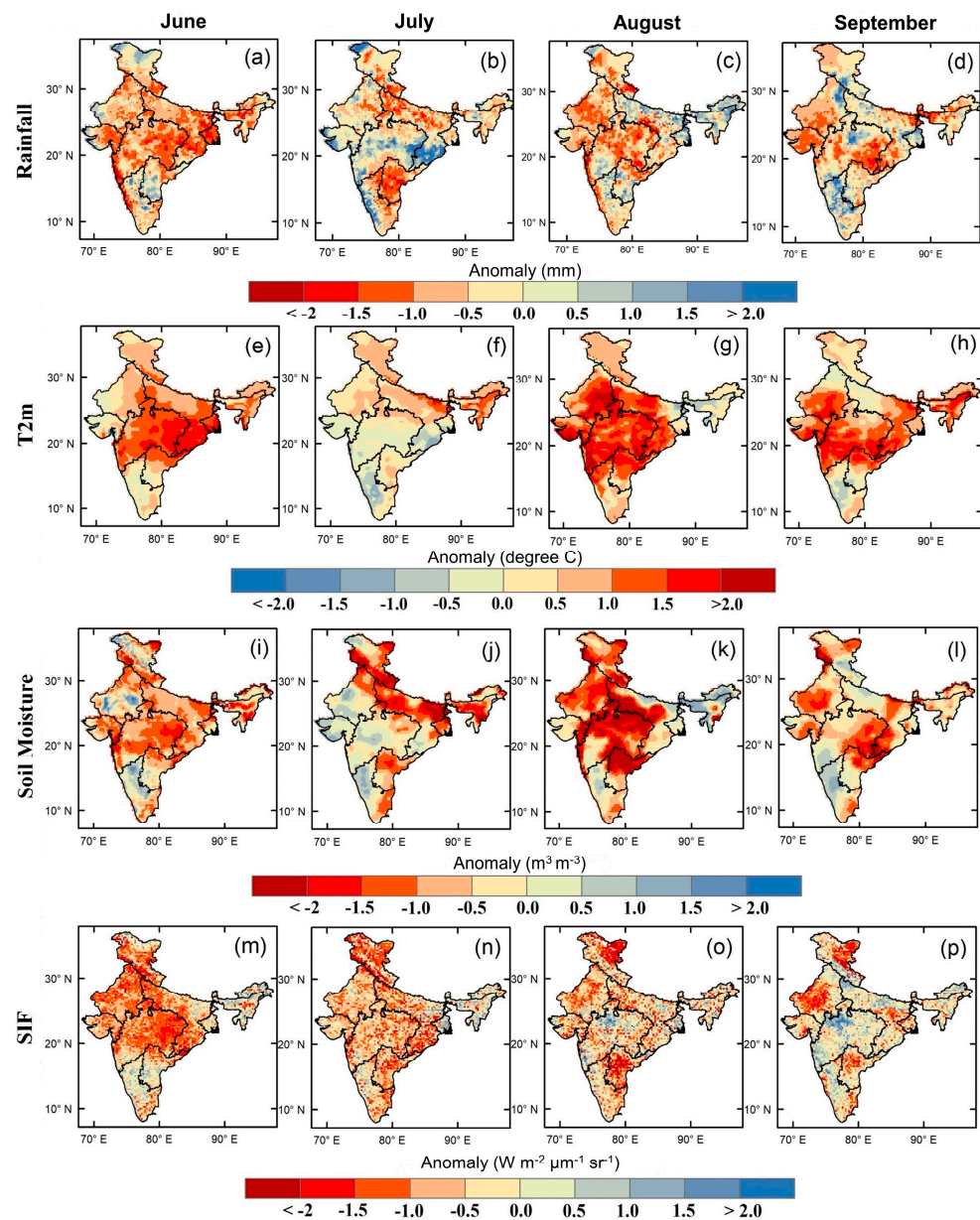


Figure 8. Spatial variation in rainfall (a–d), T2m (e–h), soil moisture (i–l), and SIF (m–p) anomalies for monsoon season (June–September) in the 2009 drought year.

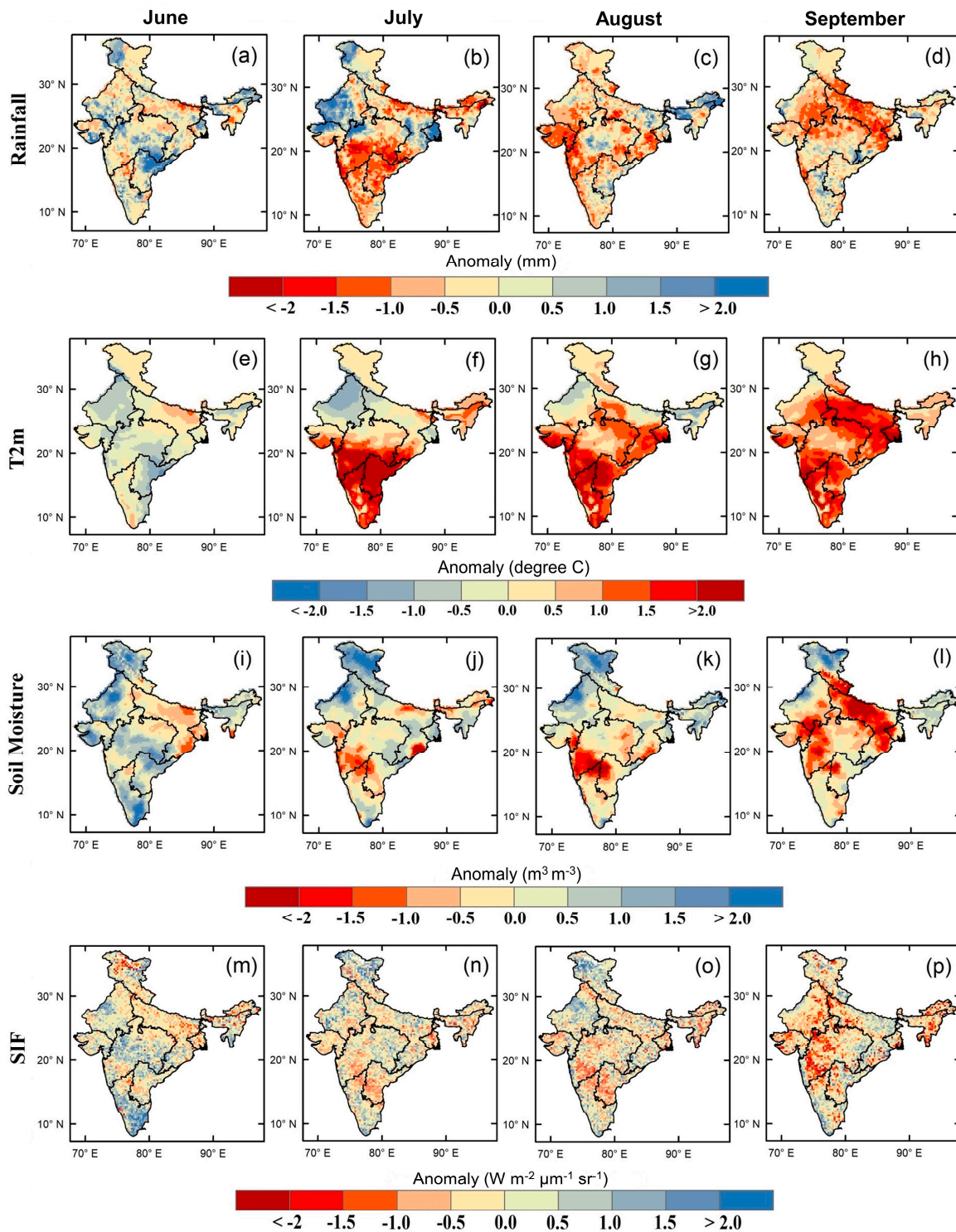


Figure 9. Spatial variation in rainfall (a–d), T2m (e–h), soil moisture (i–l), and SIF (m–p) anomalies for monsoon season (June–September) in the 2015 drought year.

In the 2009 drought year, an overall rainfall deficiency of 22% was observed, and agricultural production dropped by 16 million tons (NRAA, 2013). The spatial extent of rainfall anomalies agreed well with the 2009 drought year across India. The precipitation anomalies showed severe drought conditions (<-1.5), mainly highlighted in the northwest, central northeast, and west-central subregions, respectively. For the T2m anomaly, increased temperature exacerbated drought conditions by enhancing evaporation rates throughout

the period, which dominated in central parts of India. The anomalies observed were above normal (nearly 1.0 °C to 2.5 °C). This could lead to drying out the soil. Moreover, the soil moisture anomaly was observed to be below normal during the entire period. In the central-northeast region, the soil moisture deficit fluctuated between -0.5 and -1.5 , whereas in the west-central region, it varied from -1.0 to -2.7 during the onset of the monsoon period (in June). For the rest of the period (Jul to Sep), the severity and extent of the moisture distribution became more severe (below normal <-1.5), which mainly dominated in the northwest, central-northeast, and west-central regions. Furthermore, the spatial extent and severity of the SIF anomaly agreed well with precipitation and soil moisture anomalies across India. There was mild to severe stress observed in vegetation anomalies during JJAS. In June (early onset), the SIF anomaly fluctuated between -1.0 and -2.0 over the northwest region, whereas it varied from -1.0 to -1.5 during rest of period (July–September). In the west-central region, the values ranged from -1.0 to -2.0 , throughout the adapted period. However, the response of the SIF anomaly was observed to be inconsistent in some regions with precipitation or soil moisture. It showed less severity than precipitation or soil moisture. There might be a possible reason for this, as different vegetation types have varying levels of sensitivity to drought.

Similarly, in the 2015 drought year, the precipitation anomaly showed moderate to severe drought conditions and varied between -1.0 and -2.0 , affecting the west-central and peninsular regions in the early stage and further swift to the north-central region. The surface air temperature followed a similar spatial pattern and remained above normal (1.5 °C to 2.5 °C) from Jul to Sep. This high temperature increased evaporative demand and dried the soil. There was a lag response between meteorological variables and SIF anomalies. However, SIF showed almost consistency throughout the region with soil moisture anomalies during the entire period.

5. Discussion

The Indian Ocean witnessed a weak positive IOD event with a relatively low amplitude with El Niño over the tropical Pacific Ocean. This goes beyond conventional understanding, as a robust El Niño typically promotes the robust development of a positive Indian Ocean Dipole (IOD) through dynamic connections. This particular El Niño is commonly referred to as the cold-tongue El Niño [96,97]. For example, the distribution of SSTAs in 2015 was observed to be the result of the co-occurrence of the traditional El Niño phenomenon with the EM-II event. The association between EM-II and an intensified Walker circulation in the Indo-Pacific region leads to enhanced precipitation over the Maritime Continent and the tropical eastern Indian Ocean. Consequently, surface westerly wind anomalies occur off Java–Sumatra. As a result, EM-II is not conducive to the positive development of the IOD through the Bjerknes feedback mechanism [98,99]. This might be the possible reason for the weakening of the IOD in 2015. Additional factors contributing to the weak IOD event in 2015 could include the decadal variability in IOD events [100] and Asian summer monsoon variations [101].

We further explored and made a spatial comparison to showcase the effectiveness of land anomalies in terms of intensity and spatial coverage for the 2015 drought year. The precipitation anomalies showed severe drought-stricken-like conditions over the central northeast and peninsular region while other regions showed mild to moderate stress. A similar spatial pattern was followed by surface air temperature and soil moisture anomalies from June to September. However, the response of SIF was observed to be less severe (see Figure 9m–p) than other drought anomalies across the subregions. This might be because of ecosystem resilience or other water resource availability (i.e., canal irrigation, groundwater pumping) during drought-stricken-like conditions. In addition, different vegetation types have varying levels of sensitivity to drought. This variation in vegetation types across a region can lead to inconsistencies between SIF and precipitation and soil moisture anomalies [102–104].

Ecosystems may exhibit higher resilience or adaptive mechanisms to withstand drought conditions, while others may be more susceptible and show visible impacts at earlier stages. Furthermore, the non-uniformity in the moisture distribution over space is also a crucial aspect. Moisture deficits are often spatially heterogeneous, with some areas experiencing more severe deficits than others. This non-uniform distribution of moisture can lead to varied vegetation responses across different locations, resulting in non-linear relationships between moisture deficits and vegetation health [105,106].

6. Conclusions

The present study aims to reveal the revolutionary features of the El Niño and weak positive IOD events that occurred over the tropical Pacific and Indian Ocean, respectively, during 2009 and 2015. These events significantly influenced SST variability over the tropical Indian Ocean and rainfall distribution patterns over India. During the ENSO phases, SSTAs were observed to be above normal over the tropical Indian Ocean in the boreal summer.

The atypical distribution of SSTAs over the tropical Pacific region played a role in the formation of a relatively mild positive IOD event in the year 2015. The tropical Pacific region exhibited a combination of traditional El Niño and El Niño Modoki II phenomena, resulting in the presence of two contrasting abnormal Walker circulations across the tropical Indian Ocean. It was noted that during these events, the Indian landmass region received below-normal rainfall and experienced severe drought, which further affected vegetation photosynthesis. Traditional drought condition anomalies (precipitation, temperature, and soil moisture) agreed well with SIF anomalies in terms of severity and spatial coverage. However, the response of SIF was to be observed less severe than the other drought anomalies across the subregions because of ecosystem resilience or adaptive mechanisms to withstand drought conditions. Therefore, this teleconnection relationship (herein, SST-ISMIR-SIF) could be extended by incorporating the time lag between these variables. This inclusion of time lag may contribute to a better understanding of the diverse plant responses to SST fluctuations in the tropical Indian Ocean. In future studies, we will focus on the most recent temperature trends and patterns up to 2022, potentially focusing on emerging anomalies or noteworthy shifts. We may further extend this study with predictive modeling using an extended dataset to anticipate SST variations in subsequent years. Such forecasting studies are beneficial for the efficient use of water resources in rainfed agriculture regions in drought-stricken conditions.

Author Contributions: Conceptualization V.K. and H.-J.C.; Methodology, V.K., H.-J.C. and A.A.; Formal analysis, V.K., H.-J.C. and A.A.; Writing—original draft, V.K.; Writing—review and editing H.-J.C. and V.K.; Supervision, H.-J.C. All authors have read and agreed to the published version of this manuscript.

Funding: The scholarship of Kumar was supported by the National Science and Technology Council (NSTC), Taiwan (Project ID: 112-2121-M-006-007), and NCKU Sustainable Interdisciplinary Integrated Project, Taiwan.

Data Availability Statement: We wish to convey our deep appreciation to the India Meteorological Department (IMD) located in Pune (https://www.imdpune.gov.in/Clim_Pred_LRF_New/Gridded_Data_Download.html) for providing precipitation and surface air temperature dataset for this study (accessed on 21 October 2023). The OISST dataset was collected from the National Center for Environmental Information (<https://www.ncei.noaa.gov/data/sea-surface-temperature-optimum-interpolation/v2/access/avhrr-only/>) (accessed on 27 October 2023). Both the Niño 3.4 SST index and the dipole mode index were collected from climate time series developed by the GCOS surface pressure working group (https://psl.noaa.gov/gcos_wgsp/Timeseries/) (accessed on 16 October 2023). Wind components were obtained from the C3S climate data store (<https://cds.climate.copernicus.eu/cdsapp#!/dataset/reanalysis-era5-pressure-levels-monthly-means?tab=form>) (accessed on 2 November 2023). The soil moisture dataset was obtained from Ghent University under the GLEAM project (<https://www.gleam.eu/#downloads>) (accessed on 21 October 2023). The GOSIF is available at the Global Ecology Group's data repository on reasonable request (<http://data.globalecology.unh.edu/>) (accessed on 21 October 2023). Bathymetry data can be obtained from GEBCO gridded

bathymetry data at the British Oceanographic Data Centre (BODC) (https://www.gebco.net/data_and_products/gridded_bathymetry_data/) (accessed on 16 October 2023).

Acknowledgments: The authors express sincere gratitude to Geo-Smart Lab members, NCKU Taiwan, and Aman Rai, Department of Geography, Delhi School of Economics, University of Delhi, India, for providing valuable suggestions during this study’s execution.

Conflicts of Interest: The authors declare no conflicts of interest.

Abbreviations

IMD	India Meteorological Department
GLEAM	Global Land Evaporation Amsterdam Model
SST	Sea Surface Temperature
SIF	Solar-induced chlorophyll Fluorescence
ENSO	El Niño Southern Oscillation
WIO	Western Indian Ocean
NIO	Northern Indian Ocean
CIO	Central Indian Ocean
IOD	Indian Ocean Dipole
DMI	Dipole Mode Index

Appendix A

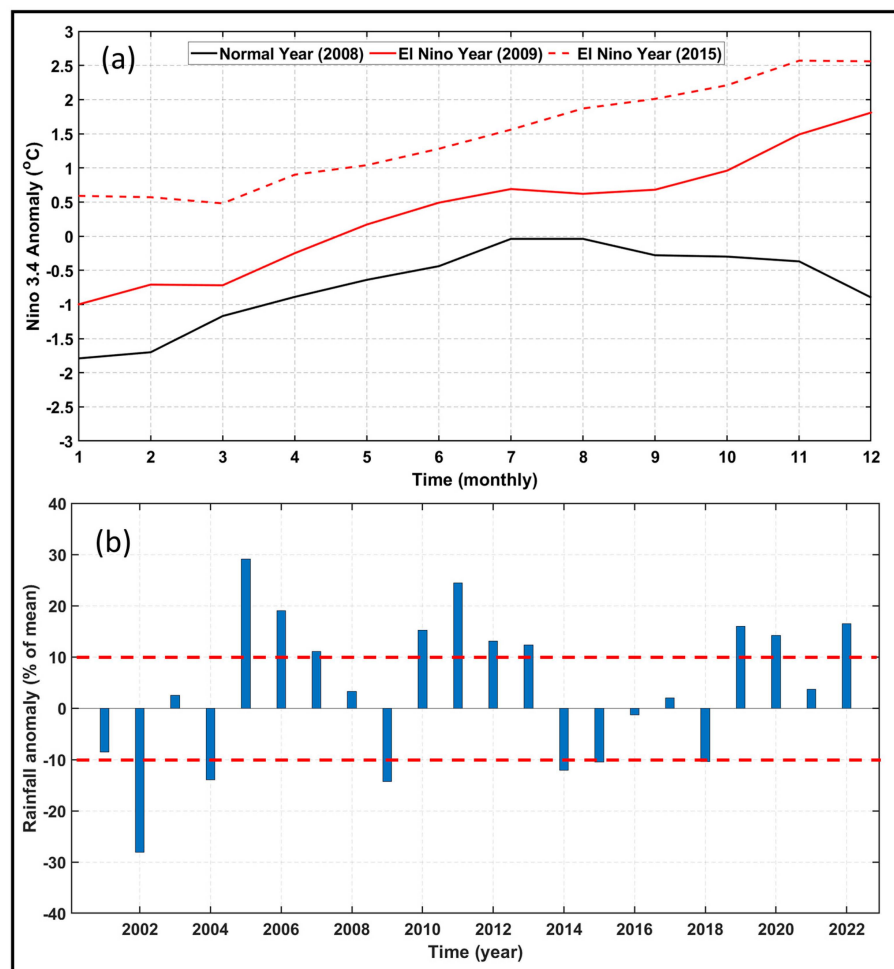


Figure A1. (a) Nino 3.4 SST anomalies during normal year and El-Nino years which depicts strong interannual variability; (b) Rainfall anomaly with excess-deficient rainfall years nationwide India from 2001 to 2022.

References

- Gonsamo, A.; Chen, J.M.; Lombardozzi, D. Global Vegetation Productivity Response to Climatic Oscillations during the Satellite Era. *Glob. Chang. Biol.* **2016**, *22*, 3414–3426. [[CrossRef](#)] [[PubMed](#)]
- O'carroll, A.G.; Armstrong, E.M.; Beggs, H.M.; Bouali, M.; Casey, K.S.; Corlett, G.K.; Dash, P.; Donlon, C.J.; Gentemann, C.L.; Høyer, J.L. Observational Needs of Sea Surface Temperature. *Front. Mar. Sci.* **2019**, *6*, 420. [[CrossRef](#)]
- Phillips, H.E.; Tandon, A.; Furue, R.; Hood, R.; Ummenhofer, C.C.; Benthuyzen, J.A.; Menezes, V.; Hu, S.; Webber, B.; Sanchez-Franks, A. Progress in Understanding of Indian Ocean Circulation, Variability, Air–Sea Exchange, and Impacts on Biogeochemistry. *Ocean Sci.* **2021**, *17*, 1677–1751. [[CrossRef](#)]
- Halpern, B.S.; Frazier, M.; Afflerbach, J.; O'Hara, C.; Katona, S.; Stewart Lowndes, J.S.; Jiang, N.; Pacheco, E.; Scarborough, C.; Polsenberg, J. Drivers and Implications of Change in Global Ocean Health over the Past Five Years. *PLoS ONE* **2017**, *12*, e0178267. [[CrossRef](#)] [[PubMed](#)]
- Reimer, J.J.; Vargas, R.; Rivas, D.; Gaxiola-Castro, G.; Hernandez-Ayon, J.M.; Lara-Lara, R. Sea Surface Temperature Influence on Terrestrial Gross Primary Production along the Southern California Current. *PLoS ONE* **2015**, *10*, e0125177. [[CrossRef](#)]
- Chen, M.; Parton, W.J.; Del Grosso, S.J.; Hartman, M.D.; Day, K.A.; Tucker, C.J.; Derner, J.D.; Knapp, A.K.; Smith, W.K.; Ojima, D.S. The Signature of Sea Surface Temperature Anomalies on the Dynamics of Semiarid Grassland Productivity. *Ecosphere* **2017**, *8*, e02069. [[CrossRef](#)]
- Zhu, Z.; Piao, S.; Xu, Y.; Bastos, A.; Ciais, P.; Peng, S. The Effects of Teleconnections on Carbon Fluxes of Global Terrestrial Ecosystems. *Geophys. Res. Lett.* **2017**, *44*, 3209–3218. [[CrossRef](#)]
- Nzabarinda, V.; Bao, A.; Xu, W.; Uwamahoro, S.; Jiang, L.; Duan, Y.; Nahayo, L.; Yu, T.; Wang, T.; Long, G. Assessment and Evaluation of the Response of Vegetation Dynamics to Climate Variability in Africa. *Sustainability* **2021**, *13*, 1234. [[CrossRef](#)]
- Wang, J.; Wang, M.; Kim, J.; Joiner, J.; Zeng, N.; Jiang, F.; Wang, H.; He, W.; Wu, M.; Chen, T. Modulation of Land Photosynthesis by the Indian Ocean Dipole: Satellite-based Observations and CMIP6 Future Projections. *Earth's Futur.* **2021**, *9*, e2020EF001942. [[CrossRef](#)]
- Ashok, K.; Guan, Z.; Yamagata, T. A Look at the Relationship between the ENSO and the Indian Ocean Dipole. *J. Meteorol. Soc. Japan. Ser. II* **2003**, *81*, 41–56. [[CrossRef](#)]
- Devi, K.N.; Sarangi, R.K. Time-Series Analysis of Chlorophyll-a, Sea Surface Temperature, and Sea Surface Height Anomalies during 2003–2014 with Special Reference to El Niño, La Niña, and Indian Ocean Dipole (IOD) Years. *Int. J. Remote Sens.* **2017**, *38*, 5626–5639. [[CrossRef](#)]
- Ashok, K.; Guan, Z.; Yamagata, T. Influence of the Indian Ocean Dipole on the Australian Winter Rainfall. *Geophys. Res. Lett.* **2003**, *30*. [[CrossRef](#)]
- Ashok, K.; Guan, Z.; Saji, N.H.; Yamagata, T. Individual and Combined Influences of ENSO and the Indian Ocean Dipole on the Indian Summer Monsoon. *J. Clim.* **2004**, *17*, 3141–3155. [[CrossRef](#)]
- Ashok, K.; Behera, S.K.; Rao, S.A.; Weng, H.; Yamagata, T. El Niño Modoki and Its Possible Teleconnection. *J. Geophys. Res. Ocean.* **2007**, *112*. [[CrossRef](#)]
- Slingo, J.M.; Annamalai, H. 1997: The El Niño of the Century and the Response of the Indian Summer Monsoon. *Mon. Weather Rev.* **2000**, *128*, 1778–1797. [[CrossRef](#)]
- Lau, N.-C.; Nath, M.J. Impact of ENSO on the Variability of the Asian–Australian Monsoons as Simulated in GCM Experiments. *J. Clim.* **2000**, *13*, 4287–4309. [[CrossRef](#)]
- Annamalai, H.; Liu, P. Response of the Asian Summer Monsoon to Changes in El Niño Properties. *Q. J. R. Meteorol. Soc. A J. Atmos. Sci. Appl. Meteorol. Phys. Oceanogr.* **2005**, *131*, 805–831. [[CrossRef](#)]
- Mishra, V.; Smoliak, B.V.; Lettenmaier, D.P.; Wallace, J.M. A Prominent Pattern of Year-to-Year Variability in Indian Summer Monsoon Rainfall. *Proc. Natl. Acad. Sci. USA* **2012**, *109*, 7213–7217. [[CrossRef](#)]
- Ashok, K.; Tejavath, C.T. The Indian Summer Monsoon Rainfall and ENSO. *Mausam* **2019**, *70*, 443–452. [[CrossRef](#)]
- Ummenhofer, C.C.; Gupta, A.S.; Li, Y.; Taschetto, A.S.; England, M.H. Multi-Decadal Modulation of the El Niño–Indian Monsoon Relationship by Indian Ocean Variability. *Environ. Res. Lett.* **2011**, *6*, 34006. [[CrossRef](#)]
- Joseph, S.; Sahai, A.K.; Chattopadhyay, R.; Goswami, B.N. Can El Niño–Southern Oscillation (ENSO) Events Modulate Intraseasonal Oscillations of Indian Summer Monsoon? *J. Geophys. Res. Atmos.* **2011**, *116*. [[CrossRef](#)]
- Power, S.B.; Smith, I.N. Weakening of the Walker Circulation and Apparent Dominance of El Niño Both Reach Record Levels, but Has ENSO Really Changed? *Geophys. Res. Lett.* **2007**, *34*. [[CrossRef](#)]
- Stachnik, J.P.; Schumacher, C. A Comparison of the Hadley Circulation in Modern Reanalyses. *J. Geophys. Res. Atmos.* **2011**, *116*. [[CrossRef](#)]
- Ashok, K.; Saji, N.H. On the Impacts of ENSO and Indian Ocean Dipole Events on Sub-Regional Indian Summer Monsoon Rainfall. *Nat. Hazards* **2007**, *42*, 273–285. [[CrossRef](#)]
- Saji, N.H.; Goswami, B.N.; Vinayachandran, P.N.; Yamagata, T. A Dipole Mode in the Tropical Indian Ocean. *Nature* **1999**, *401*, 360–363. [[CrossRef](#)] [[PubMed](#)]
- Zhang, W.; Wang, Y.; Jin, F.; Stuecker, M.F.; Turner, A.G. Impact of Different El Niño Types on the El Niño/IOD Relationship. *Geophys. Res. Lett.* **2015**, *42*, 8570–8576. [[CrossRef](#)]
- Han, W.; Vialard, J.; McPhaden, M.J.; Lee, T.; Masumoto, Y.; Feng, M.; De Ruijter, W.P.M. Indian Ocean Decadal Variability: A Review. *Bull. Am. Meteorol. Soc.* **2014**, *95*, 1679–1703. [[CrossRef](#)]

28. Ashok, K.; Guan, Z.; Yamagata, T. Impact of the Indian Ocean Dipole on the Relationship between the Indian Monsoon Rainfall and ENSO. *Geophys. Res. Lett.* **2001**, *28*, 4499–4502. [[CrossRef](#)]
29. Yamagata, T.; Behera, S.K.; Luo, J.-J.; Masson, S.; Jury, M.R.; Rao, S.A. Coupled Ocean-Atmosphere Variability in the Tropical Indian Ocean. *Earth's Clim. Ocean. Interact. Geophys. Monogr* **2004**, *147*, 189–212.
30. Luo, J.-J.; Zhang, R.; Behera, S.K.; Masumoto, Y.; Jin, F.-F.; Lukas, R.; Yamagata, T. Interaction between El Nino and Extreme Indian Ocean Dipole. *J. Clim.* **2010**, *23*, 726–742. [[CrossRef](#)]
31. Behera, S.K.; Luo, J.-J.; Masson, S.; Delecluse, P.; Gualdi, S.; Navarra, A.; Yamagata, T. Paramount Impact of the Indian Ocean Dipole on the East African Short Rains: A CGCM Study. *J. Clim.* **2005**, *18*, 4514–4530. [[CrossRef](#)]
32. Gupta, V.; Jain, M.K. Unravelling the Teleconnections between ENSO and Dry/Wet Conditions over India Using Nonlinear Granger Causality. *Atmos. Res.* **2021**, *247*, 105168. [[CrossRef](#)]
33. Mishra, A.K.; Kumar, P.; Dubey, A.K.; Jha, S.K.; Sein, D.V.; Cabos, W. Demonstrating the Asymmetry of the Indian Ocean Dipole Response in Regional Earth System Model of CORDEX-SA. *Atmos. Res.* **2022**, *273*, 106182. [[CrossRef](#)]
34. Saji, N.H.; Yamagata, T. Structure of SST and Surface Wind Variability during Indian Ocean Dipole Mode Events: COADS Observations. *J. Clim.* **2003**, *16*, 2735–2751. [[CrossRef](#)]
35. Mishra, V.; Tiwari, A.D.; Aadhar, S.; Shah, R.; Xiao, M.; Pai, D.S.; Lettenmaier, D. Drought and Famine in India, 1870–2016. *Geophys. Res. Lett.* **2019**, *46*, 2075–2083. [[CrossRef](#)]
36. Krishnamurthy, V.; Shukla, J. Intraseasonal and Interannual Variability of Rainfall over India. *J. Clim.* **2000**, *13*, 4366–4377. [[CrossRef](#)]
37. Parthasarathy, B.; Munot, A.A.; Kothawale, D.R. All-India Monthly and Seasonal Rainfall Series: 1871–1993. *Theor. Appl. Climatol.* **1994**, *49*, 217–224. [[CrossRef](#)]
38. Goswami, B.N.; Venugopal, V.; Sengupta, D.; Madhusoodanan, M.S.; Xavier, P.K. Increasing Trend of Extreme Rain Events over India in a Warming Environment. *Science* **2006**, *314*, 1442–1445. [[CrossRef](#)]
39. Roxy, M.K.; Ritika, K.; Terray, P.; Murtugudde, R.; Ashok, K.; Goswami, B.N. Drying of Indian Subcontinent by Rapid Indian Ocean Warming and a Weakening Land-Sea Thermal Gradient. *Nat. Commun.* **2015**, *6*, 7423. [[CrossRef](#)]
40. Singh, D.; Tsiang, M.; Rajaratnam, B.; Diffenbaugh, N.S. Observed Changes in Extreme Wet and Dry Spells during the South Asian Summer Monsoon Season. *Nat. Clim. Chang.* **2014**, *4*, 456–461. [[CrossRef](#)]
41. Niranjana Kumar, K.; Rajeevan, M.; Pai, D.S.; Srivastava, A.K.; Preethi, B. On the Observed Variability of Monsoon Droughts over India. *Weather Clim. Extrem.* **2013**, *1*, 42–50. [[CrossRef](#)]
42. Turner, A.G.; Annamalai, H. Climate Change and the South Asian Summer Monsoon. *Nat. Clim. Chang.* **2012**, *2*, 587–595. [[CrossRef](#)]
43. Christian, J.I.; Basara, J.B.; Hunt, E.D.; Otkin, J.A.; Furtado, J.C.; Mishra, V.; Xiao, X.; Randall, R.M. Global Distribution, Trends, and Drivers of Flash Drought Occurrence. *Nat. Commun.* **2021**, *12*, 6330. [[CrossRef](#)] [[PubMed](#)]
44. Orth, R.; Seneviratne, S.I. Variability of Soil Moisture and Sea Surface Temperatures Similarly Important for Warm-Season Land Climate in the Community Earth System Model. *J. Clim.* **2017**, *30*, 2141–2162. [[CrossRef](#)]
45. Yan, B.; Mao, J.; Shi, X.; Hoffman, F.M.; Notaro, M.; Zhou, T.; McDowell, N.; Dickinson, R.E.; Xu, M.; Gu, L. Predictability of Tropical Vegetation Greenness Using Sea Surface Temperatures. *Environ. Res. Commun.* **2019**, *1*, 31003. [[CrossRef](#)]
46. Huang, M.; Wang, Z.; Wang, S.; Gu, F.; Gong, H.; Hao, M.; Shao, Y. Global Vegetation Productivity Responses to the West Pacific Warm Pool. *Sci. Total Environ.* **2019**, *655*, 641–651. [[CrossRef](#)] [[PubMed](#)]
47. Asoka, A.; Mishra, V. Prediction of Vegetation Anomalies to Improve Food Security and Water Management in India. *Geophys. Res. Lett.* **2015**, *42*, 5290–5298. [[CrossRef](#)]
48. Sharma, A.; Goyal, M.K. Assessment of Ecosystem Resilience to Hydroclimatic Disturbances in India. *Glob. Chang. Biol.* **2018**, *24*, e432–e441. [[CrossRef](#)]
49. Nayak, R.K.; Patel, N.R.; Dadhwal, V.K. Inter-annual Variability and Climate Control of Terrestrial Net Primary Productivity over India. *Int. J. Climatol.* **2013**, *33*, 132–142. [[CrossRef](#)]
50. Banger, K.; Tian, H.; Tao, B.; Ren, W.; Pan, S.; Dangal, S.; Yang, J. Terrestrial Net Primary Productivity in India during 1901–2010: Contributions from Multiple Environmental Changes. *Clim. Chang.* **2015**, *132*, 575–588. [[CrossRef](#)]
51. Bala, G.; Joshi, J.; Chaturvedi, R.K.; Gangamani, H.V.; Hashimoto, H.; Nemani, R. Trends and Variability of AVHRR-Derived NPP in India. *Remote Sens.* **2013**, *5*, 810–829. [[CrossRef](#)]
52. Rao, A.S.; Bala, G.; Ravindranath, N.H.; Nemani, R. Multi-Model Assessment of Trends, Variability and Drivers of Terrestrial Carbon Uptake in India. *J. Earth Syst. Sci.* **2019**, *128*, 99. [[CrossRef](#)]
53. Kulkarni, S.S.; Wardlaw, B.D.; Bayissa, Y.A.; Tadesse, T.; Svoboda, M.D.; Gedam, S.S. Developing a Remote Sensing-Based Combined Drought Indicator Approach for Agricultural Drought Monitoring over Marathwada, India. *Remote Sens.* **2020**, *12*, 2091. [[CrossRef](#)]
54. Kumar, A.; Pandey, V.; Shekh, A.M.; Lunagaria, M.M.; Patel, H.R. The Impact of El Nino and La Nina (ENSO) on Monsoon Rainfall in Gujarat. *J. Agrometeorol.* **2012**, *14*, 151–156.
55. Kim, I.-W.; Stuecker, M.F.; Timmermann, A.; Zeller, E.; Kug, J.-S.; Park, S.-W.; Kim, J.-S. Tropical Indo-Pacific SST Influences on Vegetation Variability in Eastern Africa. *Sci. Rep.* **2021**, *11*, 10462. [[CrossRef](#)] [[PubMed](#)]
56. Huber, S.; Fensholt, R. Analysis of Teleconnections between AVHRR-Based Sea Surface Temperature and Vegetation Productivity in the Semi-Arid Sahel. *Remote Sens. Environ.* **2011**, *115*, 3276–3285. [[CrossRef](#)]

57. Roxy, M. Sensitivity of Precipitation to Sea Surface Temperature over the Tropical Summer Monsoon Region—And Its Quantification. *Clim. Dyn.* **2014**, *43*, 1159–1169. [[CrossRef](#)]
58. Huang, B.; Liu, C.; Banzon, V.; Freeman, E.; Graham, G.; Hankins, B.; Smith, T.; Zhang, H.-M. Improvements of the Daily Optimum Interpolation Sea Surface Temperature (DOISST) Version 2.1. *J. Clim.* **2021**, *34*, 2923–2939. [[CrossRef](#)]
59. Reynolds, R.W.; Smith, T.M.; Liu, C.; Chelton, D.B.; Casey, K.S.; Schlax, M.G. Daily High-Resolution-Blended Analyses for Sea Surface Temperature. *J. Clim.* **2007**, *20*, 5473–5496. [[CrossRef](#)]
60. Banzon, V.; Smith, T.M.; Chin, T.M.; Liu, C.; Hankins, W. A Long-Term Record of Blended Satellite and in Situ Sea-Surface Temperature for Climate Monitoring, Modeling and Environmental Studies. *Earth Syst. Sci. Data* **2016**, *8*, 165–176. [[CrossRef](#)]
61. Wilson, S.S.; Joseph, P.V.; Mohanakumar, K.; Johannessen, O.M. Interannual and Long Term Variability of Low Level Jetstream of the Asian Summer Monsoon. *Tellus A Dyn. Meteorol. Oceanogr.* **2018**, *70*, 1–9. [[CrossRef](#)]
62. Nandini, G.; Vinoj, V.; Pandey, S.K. Arabian Sea Aerosol-Indian Summer Monsoon Rainfall Relationship and Its Modulation by El-Nino Southern Oscillation. *Npj Clim. Atmos. Sci.* **2022**, *5*, 25. [[CrossRef](#)]
63. Hersbach, H.; Bell, B.; Berrisford, P.; Hirahara, S.; Horányi, A.; Muñoz-Sabater, J.; Nicolas, J.; Peubey, C.; Radu, R.; Schepers, D. The ERA5 Global Reanalysis. *Q. J. R. Meteorol. Soc.* **2020**, *146*, 1999–2049. [[CrossRef](#)]
64. Shepard, D.S. Computer Mapping: The SYMAP Interpolation Algorithm. In *Spatial Statistics and Models*; Gaile, G.L., Willmott, C.J., Eds.; Springer: Dordrecht, The Netherlands, 1984; pp. 133–145, ISBN 978-94-017-3048-8.
65. Pai, D.S.; Rajeevan, M.; Sreejith, O.P.; Mukhopadhyay, B.; Satbha, N.S. Development of a New High Spatial Resolution (0.25 × 0.25) Long Period (1901–2010) Daily Gridded Rainfall Data Set over India and Its Comparison with Existing Data Sets over the Region. *Mausam* **2014**, *65*, 1–18. [[CrossRef](#)]
66. Srivastava, A.K.; Rajeevan, M.; Kshirsagar, S.R. Development of a High Resolution Daily Gridded Temperature Data Set (1969–2005) for the Indian Region. *Atmos. Sci. Lett.* **2009**, *10*, 249–254. [[CrossRef](#)]
67. Pai, D.S.; Sridhar, L.; Badwaik, M.R.; Rajeevan, M. Analysis of the Daily Rainfall Events over India Using a New Long Period (1901–2010) High Resolution (0.25° × 0.25°) Gridded Rainfall Data Set. *Clim. Dyn.* **2015**, *45*, 755–776. [[CrossRef](#)]
68. Shah, D.; Mishra, V. Drought Onset and Termination in India. *J. Geophys. Res. Atmos.* **2020**, *125*, e2020JD032871. [[CrossRef](#)]
69. Kumar, R.; Mishra, V. Decline in Surface Urban Heat Island Intensity in India during Heatwaves. *Environ. Res. Commun.* **2019**, *1*, 31001. [[CrossRef](#)]
70. Mishra, A.K.; Ines, A.V.M.; Das, N.N.; Khedun, P. Anatomy of a Local Scale Drought. In Proceedings of the AGU Fall Meeting Abstracts; AGU: Washington, DC, USA, 2014; p. H31M-06.
71. Martens, B.; Miralles, D.G.; Lievens, H.; Van Der Schalie, R.; De Jeu, R.A.M.; Fernández-Prieto, D.; Beck, H.E.; Dorigo, W.A.; Verhoest, N.E.C. GLEAM v3: Satellite-Based Land Evaporation and Root-Zone Soil Moisture. *Geosci. Model Dev.* **2017**, *10*, 1903–1925. [[CrossRef](#)]
72. Martens, B.; Miralles, D.; Lievens, H.; Fernández-Prieto, D.; Verhoest, N.E.C. Improving Terrestrial Evaporation Estimates over Continental Australia through Assimilation of SMOS Soil Moisture. *Int. J. Appl. Earth Obs. Geoinf.* **2016**, *48*, 146–162. [[CrossRef](#)]
73. Miralles, D.G.; Holmes, T.R.H.; De Jeu, R.A.M.; Gash, J.H.; Meesters, A.; Dolman, A.J. Global Land-Surface Evaporation Estimated from Satellite-Based Observations. *Hydrol. Earth Syst. Sci.* **2011**, *15*, 453–469. [[CrossRef](#)]
74. Priestley, C.H.B.; Taylor, R.J. On the Assessment of Surface Heat Flux and Evaporation Using Large-Scale Parameters. *Mon. Weather Rev.* **1972**, *100*, 81–92. [[CrossRef](#)]
75. Li, X.; Xiao, J. A Global, 0.05-Degree Product of Solar-Induced Chlorophyll Fluorescence Derived from OCO-2, MODIS, and Reanalysis Data. *Remote Sens.* **2019**, *11*, 517. [[CrossRef](#)]
76. Qiu, R.; Han, G.; Ma, X.; Xu, H.; Shi, T.; Zhang, M. A Comparison of OCO-2 SIF, MODIS GPP, and GOSIF Data from Gross Primary Production (GPP) Estimation and Seasonal Cycles in North America. *Remote Sens.* **2020**, *12*, 258. [[CrossRef](#)]
77. Li, X.; Xiao, J. Mapping Photosynthesis Solely from Solar-Induced Chlorophyll Fluorescence: A Global, Fine-Resolution Dataset of Gross Primary Production Derived from OCO-2. *Remote Sens.* **2019**, *11*, 2563. [[CrossRef](#)]
78. Xu, S.; Atherton, J.; Riikonen, A.; Zhang, C.; Oivukkamäki, J.; MacArthur, A.; Honkavaara, E.; Hakala, T.; Koivumäki, N.; Liu, Z. Structural and Photosynthetic Dynamics Mediate the Response of SIF to Water Stress in a Potato Crop. *Remote Sens. Environ.* **2021**, *263*, 112555. [[CrossRef](#)]
79. Siegmann, B.; Cendrero-Mateo, M.P.; Cogliati, S.; Damm, A.; Gamon, J.; Herrera, D.; Jedmowski, C.; Junker-Frohn, L.V.; Kraska, T.; Muller, O. Downscaling of Far-Red Solar-Induced Chlorophyll Fluorescence of Different Crops from Canopy to Leaf Level Using a Diurnal Data Set Acquired by the Airborne Imaging Spectrometer HyPlant. *Remote Sens. Environ.* **2021**, *264*, 112609. [[CrossRef](#)] [[PubMed](#)]
80. Xiao, J.; Li, X.; He, B.; Arain, M.A.; Beringer, J.; Desai, A.R.; Emmel, C.; Hollinger, D.Y.; Krasnova, A.; Mammarella, I. Solar-induced Chlorophyll Fluorescence Exhibits a Universal Relationship with Gross Primary Productivity across a Wide Variety of Biomes. *Glob. Chang. Biol.* **2019**, *25*, e4–e6. [[CrossRef](#)]
81. Xu, L.; Samanta, A.; Costa, M.H.; Ganguly, S.; Nemani, R.R.; Myneni, R.B. Widespread Decline in Greenness of Amazonian Vegetation Due to the 2010 Drought. *Geophys. Res. Lett.* **2011**, *38*. [[CrossRef](#)]
82. Zhou, L.; Tian, Y.; Myneni, R.B.; Ciaia, P.; Saatchi, S.; Liu, Y.Y.; Piao, S.; Chen, H.; Vermote, E.F.; Song, C. Widespread Decline of Congo Rainforest Greenness in the Past Decade. *Nature* **2014**, *509*, 86–90. [[CrossRef](#)] [[PubMed](#)]

83. Rayner, N.A.A.; Parker, D.E.; Horton, E.B.; Folland, C.K.; Alexander, L.V.; Rowell, D.P.; Kent, E.C.; Kaplan, A. Global Analyses of Sea Surface Temperature, Sea Ice, and Night Marine Air Temperature since the Late Nineteenth Century. *J. Geophys. Res. Atmos.* **2003**, *108*. [[CrossRef](#)]
84. Minola, L.; Zhang, F.; Azorin-Molina, C.; Pirooz, A.A.S.; Flay, R.G.J.; Hersbach, H.; Chen, D. Near-Surface Mean and Gust Wind Speeds in ERA5 across Sweden: Towards an Improved Gust Parametrization. *Clim. Dyn.* **2020**, *55*, 887–907. [[CrossRef](#)]
85. Saji, N.H.; Yamagata, T. Possible Impacts of Indian Ocean Dipole Mode Events on Global Climate. *Clim. Res.* **2003**, *25*, 151–169. [[CrossRef](#)]
86. Murtugudde, R.; Seager, R.; Thoppil, P. Arabian Sea Response to Monsoon Variations. *Paleoceanography* **2007**, *22*. [[CrossRef](#)]
87. Kantha, L.H.; Clayson, C.A. An Improved Mixed Layer Model for Geophysical Applications. *J. Geophys. Res. Ocean.* **1994**, *99*, 25235–25266. [[CrossRef](#)]
88. Mohd Akhir, M.F.; Zakaria, N.Z.; Tangang, F. Intermonsoon Variation of Physical Characteristics and Current Circulation along the East Coast of Peninsular Malaysia. *Int. J. Oceanogr.* **2014**, *2014*, 527587. [[CrossRef](#)]
89. Yanagi, T.; Sachoemar, S.I.; Takao, T.; Fujiwara, S. Seasonal Variation of Stratification in the Gulf of Thailand. *J. Oceanogr.* **2001**, *57*, 461–470. [[CrossRef](#)]
90. Muhammad, S.; Memon, A.A.; Muneeb, M.; Ghauri, B. Seasonal and Spatial Patterns of SST in the Northern Arabian Sea during 2001–2012. *Egypt. J. Remote Sens. Sp. Sci.* **2016**, *19*, 17–22. [[CrossRef](#)]
91. Zhang, Y.; Du, Y. Extreme IOD Induced Tropical Indian Ocean Warming in 2020. *Geosci. Lett.* **2021**, *8*, 37. [[CrossRef](#)]
92. Park, K.-A.; Lee, E.-Y.; Chang, E.; Hong, S. Spatial and Temporal Variability of Sea Surface Temperature and Warming Trends in the Yellow Sea. *J. Mar. Syst.* **2015**, *143*, 24–38. [[CrossRef](#)]
93. Nicholls, N. All-India Summer Monsoon Rainfall and Sea Surface Temperatures around Northern Australia and Indonesia. *J. Clim.* **1995**, *8*, 1463–1467. [[CrossRef](#)]
94. Saha, K. Zonal Anomaly of Sea Surface Temperature in Equatorial Indian Ocean and Its Possible Effect upon Monsoon Circulation. *Tellus* **1970**, *22*, 403–409. [[CrossRef](#)]
95. Shukla, J. Effect of Arabian Sea-Surface Temperature Anomaly on Indian Summer Monsoon: A Numerical Experiment with the GFDL Model. *J. Atmos. Sci.* **1975**, *32*, 503–511. [[CrossRef](#)]
96. Liu, L.; Yang, G.; Zhao, X.; Feng, L.; Han, G.; Wu, Y.; Yu, W. Why Was the Indian Ocean Dipole Weak in the Context of the Extreme El Niño in 2015? *J. Clim.* **2017**, *30*, 4755–4761. [[CrossRef](#)]
97. Zhu, J.; Huang, B.; Kumar, A.; Kinter, J.L., III. Seasonality in Prediction Skill and Predictable Pattern of Tropical Indian Ocean SST. *J. Clim.* **2015**, *28*, 7962–7984. [[CrossRef](#)]
98. Liu, L.; Xie, S.-P.; Zheng, X.-T.; Li, T.; Du, Y.; Huang, G.; Yu, W.-D. Indian Ocean Variability in the CMIP5 Multi-Model Ensemble: The Zonal Dipole Mode. *Clim. Dyn.* **2014**, *43*, 1715–1730. [[CrossRef](#)]
99. Liu, L.; Yu, W.; Li, T. Dynamic and Thermodynamic Air–Sea Coupling Associated with the Indian Ocean Dipole Diagnosed from 23 WCRP CMIP3 Models. *J. Clim.* **2011**, *24*, 4941–4958. [[CrossRef](#)]
100. Ashok, K.; Chan, W.; Motoi, T.; Yamagata, T. Decadal Variability of the Indian Ocean Dipole. *Geophys. Res. Lett.* **2004**, *31*. [[CrossRef](#)]
101. Cai, W.; Zheng, X.-T.; Weller, E.; Collins, M.; Cowan, T.; Lengaigne, M.; Yu, W.; Yamagata, T. Projected Response of the Indian Ocean Dipole to Greenhouse Warming. *Nat. Geosci.* **2013**, *6*, 999–1007. [[CrossRef](#)]
102. Anderegg, W.R.L.; Flint, A.; Huang, C.; Flint, L.; Berry, J.A.; Davis, F.W.; Sperry, J.S.; Field, C.B. Tree Mortality Predicted from Drought-Induced Vascular Damage. *Nat. Geosci.* **2015**, *8*, 367–371. [[CrossRef](#)]
103. Chaves, M.M.; Maroco, J.P.; Pereira, J.S. Understanding Plant Responses to Drought—From Genes to the Whole Plant. *Funct. Plant Biol.* **2003**, *30*, 239–264. [[CrossRef](#)]
104. McDowell, N.; Pockman, W.T.; Allen, C.D.; Breshears, D.D.; Cobb, N.; Kolb, T.; Plaut, J.; Sperry, J.; West, A.; Williams, D.G. Mechanisms of Plant Survival and Mortality during Drought: Why Do Some Plants Survive While Others Succumb to Drought? *New Phytol.* **2008**, *178*, 719–739. [[CrossRef](#)]
105. Anderegg, W.R.L.; Schwalm, C.; Biondi, F.; Camarero, J.J.; Koch, G.; Litvak, M.; Ogle, K.; Shaw, J.D.; Shevliakova, E.; Williams, A.P. Pervasive Drought Legacies in Forest Ecosystems and Their Implications for Carbon Cycle Models. *Science* **2015**, *349*, 528–532. [[CrossRef](#)]
106. Huxman, T.E.; Snyder, K.A.; Tissue, D.; Leffler, A.J.; Ogle, K.; Pockman, W.T.; Sandquist, D.R.; Potts, D.L.; Schwinning, S. Precipitation Pulses and Carbon Fluxes in Semiarid and Arid Ecosystems. *Oecologia* **2004**, *141*, 254–268. [[CrossRef](#)]

Disclaimer/Publisher’s Note: The statements, opinions and data contained in all publications are solely those of the individual author(s) and contributor(s) and not of MDPI and/or the editor(s). MDPI and/or the editor(s) disclaim responsibility for any injury to people or property resulting from any ideas, methods, instructions or products referred to in the content.